Original Article

JCBFM

Journal of Cerebral Blood Flow & Metabolism
2020, Vol. 40(1) 100–115

DOI: 10.1177/0271678X18803948
journals.sagepub.com/home/jcbfm
SAGE

Altered hemodynamics contribute to local but not remote functional connectivity disruption due to glioma growth

Inema E Orukari[1], Joshua S Siegel[2], Nicole M Warrington[3], Grant A Baxter[4], Adam Q Bauer[4], Joshua S Shimony[4], Joshua B Rubin[3,5] and Joseph P Culver[1,4,6]

Abstract

Glioma growth can cause pervasive changes in the functional connectivity (FC) of brain networks, which has been associated with re-organization of brain functions and development of functional deficits in patients. Mechanisms underlying functional re-organization in brain networks are not understood and efforts to utilize functional imaging for surgical planning, or as a biomarker of functional outcomes are confounded by the heterogeneity in available human data. Here we apply multiple imaging modalities in a well-controlled murine model of glioma with extensive validation using human data to explore mechanisms of FC disruption due to glioma growth. We find gliomas cause both local and distal changes in FC. FC changes in networks proximal to the tumor occur secondary to hemodynamic alterations but surprisingly, remote FC changes are independent of hemodynamic mechanisms. Our data strongly implicate hemodynamic alterations as the main driver of local changes in measurements of FC in patients with glioma.

Keywords

Functional connectivity, glioma, hemodynamic lags, mouse model, neurovascular uncoupling

Received 25 February 2018; Revised 21 June 2018; Accepted 29 July 2018

Introduction

Glioma growth causes diffuse reorganization of functional brain networks.[1] These network alterations have been associated with the development of motor[2] and cognitive[3] deficits and changes in functional localization.[4] Consequently, functional connectivity (FC) analysis of brain networks is a promising technique for both prognosticating risk of functional deficits and pre-surgical mapping in glioma patients. FC is a measure of neural activity synchrony between brain regions.[5,6] Brain regions in the same network tend to have high degrees of FC. Before FC analysis can be established in the setting of gliomas, the mechanisms of how gliomas drive FC change need to be delineated.

Unfortunately, studies of FC in patients with glioma are complicated by the heterogeneity in tumor characteristics, such as type and location. Tumor characteristics in mice can be better controlled.[7] Thus, mouse studies provide an opportunity to investigate

[1]Department of Biomedical Engineering, Washington University in St. Louis, St. Louis, MO, USA
[2]Department of Neurology, Washington University in St. Louis, St. Louis, MO, USA
[3]Department of Pediatrics, Washington University in St. Louis, St Louis, MO, USA
[4]Mallinckrodt Institute of Radiology, Washington University in St. Louis, St Louis, MO, USA
[5]Department of Neuroscience, Washington University in St. Louis, St Louis, MO, USA
[6]Department of Physics, Washington University in St. Louis, St. Louis, MO, USA

The last two authors contributed equally to this work.

Corresponding author:
Inema E Orukari, Department of Biomedical Engineering, Washington University School of Medicine, 4515 McKinley Ave, Room 2318, St. Louis, MO 63110, USA.
Email: inema.orukari@wustl.edu

mechanisms of FC change in the context of gliomas with detailed control over size, shape, location and type of tumor. However, mapping FC in mice is challenging. The small size of the mouse brain makes functional connectivity magnetic resonance imaging (fcMRI) difficult to perform due to low signal-to-noise ratios and logistics.[8] Functional connectivity optical intrinsic signal (fcOIS) imaging is an alternative approach to study FC in mice.[9] fcOIS is a relatively simple optical reflectance imaging technique that can be used to access brain dynamics and FC through the intact skull. fcOIS has been successfully applied to mouse models of Alzheimer's disease[10] and stroke.[11] Since fcOIS and fcMRI use similar contrasts (changes in hemoglobin concentrations) and analysis, findings in mice with fcOIS can be readily extended to human fcMRI studies. Therefore, we undertook the following investigations to establish the relevance and reliability of an intracranial murine xenograft model of glioblastoma (GBM) in relation to fcMRI findings in patients with gliomas.

We hypothesized GBM cells would have effects on FC that are not restricted to the local area of the tumor. To test this hypothesis, we developed FC metrics allowing us to assess widespread changes in FC in a quantitative manner. Additionally, we hypothesized hemodynamic changes may explain some of the FC changes due to glioma growth, since gliomas are known to have abnormal neo-vasculature. To test this hypothesis, we measured several hemodynamic parameters, including cerebral blood flow (CBF), average spectral power of hemodynamic fluctuations, and hemodynamic lags. To validate the relevance of our findings to human glioma, we directly tested if key findings translated to a cohort of 27 glioma patients with resting-state functional MRI (R-fMRI) data.

Materials and methods

Ethics statement

All animal studies were approved by the Washington University School of Medicine Animal Studies Committee under guidelines and regulations consistent with the Guide for the Care and Use of Laboratory Animals, Public Health Service Policy on Humane Care and Use of Laboratory Animals, and the Animal Welfare Act and Animal Welfare Regulations. Animal reporting is according to ARRIVE guidelines. All human studies were approved by the Washington University School of Medicine Internal Review Board. All patients provided informed consent for participation in an NIH-funded neurosurgery tumor database (CONDR NIH 5R01NS066905) in accordance with the Helsinki declaration.

Mouse model methods

Cell culture. U87MG cells obtained from ATCC were grown in MEM alpha with 10% fetal bovine serum and 1% penicillin/streptomycin. The cells were infected with lentivirus encoding an enhanced green fluorescence protein (eGFP)-firefly luciferase transgene (U87-GL), which enabled quantification of xenograft growth by bioluminescence imaging.[12] U87-GL cells were then engineered to overexpress a catalytically dead phosphodiesterase PDE7B construct as described previously.[13] These cells are phenotypically similar to wildtype U87MG cells.

Animal preparation. Female *Foxn1^{nu}* athymic nude mice (8–10 weeks of age, 18–26 g) were used in all experiments. For U87-GL cell injections, mice were anesthetized with 2% isoflurane and fixed in a stereotactic frame (Kopf Instruments). After a midline scalp incision, a burr hole (< 0.5 mm diameter) was made in the skull over right somatosensory forepaw cortex using a dental drill. A 31 gauge 10-µl Hamilton syringe was positioned and inserted into the right hemisphere using the following coordinates relative to bregma: anteroposterior $= +0.5$ mm, mediolateral $= +2.15$ to $+2.2$mm, and dorsoventral $= -0.5$ to -0.6 mm. A nanoinjector pump (Stoelting) was used to infuse 5×10^5 cells in 2 µl of phosphate-buffered saline (PBS) at a rate of 0.1–0.2 µl/min. Following injection, the needle was left in place for 5–10 min to ensure complete diffusion of the cells. Mice injected with 2 µl of PBS served as sham controls. The incision was closed with a 4–0 nylon suture and triple antibiotic ointment was applied topically. After a one-week recovery, Plexiglass cranial windows were fixed to the skull using dental cement (C&B-Metabond) per published protocols.[14,15]

Histology. Eight weeks post-injection (PI), mice were transcardially perfused with PBS and then 4% paraformaldehyde. Brains were removed, placed in 4% paraformaldehyde overnight, then 30% sucrose overnight. Fixed, dehydrated brains were paraffin embedded. Sagittal slices were stained with hematoxylin and eosin (H&E).

In vivo mouse imaging. To measure tumor burden, we used both bioluminescence imaging (BLI) and magnetic resonance imaging (MRI). BLI was performed as previously described.[16] MRI data were collected on a 4.7 T small animal MRI system (Agilent Technologies) as described previously.[17]

To perform functional brain imaging, we used optical intrinsic signal imaging (OISI) and laser speckle contrast imaging (LCSI). OISI converts changes in diffuse reflected light into fluctuations in hemoglobin concentration using the modified Beer–Lambert law per

published protocols.[9] LCSI transforms fluctuations in speckle patterns, due to highly coherent light illuminating perfused brain tissue, into a relative index of instantaneous CBF using a 9×9 kernel as previously described.[18]

We provide detailed descriptions of the methods for BLI, MRI, OISI, and LCSI in the supplementary materials section.

FC analysis. Fourteen seed locations were positioned at coordinates expected to correspond to the left and right motor, forelimb somatosensory, hindlimb somatosensory, barrel somatosensory, retrosplenial, parietal, and visual cortices using a histological atlas.[19] Seed time traces were calculated by averaging the time courses in each pixel within 0.25 mm of a seed locus. FC maps were created by calculating the Pearson's R correlation coefficient between each seed's time trace and those in every brain pixel. The Pearson's R correlation coefficients were converted to Fisher z-measures prior to group averaging and statistical analysis using the following equation

$$z(r) = \operatorname{arctanh}(r) \quad (1)$$

where r is the Pearson's R correlation coefficients.

The similarity metric was obtained by calculating the Pearson's R correlation coefficient between a subject-specific FC map and a corresponding reference FC map.[20] The group-average FC maps for sham-injected mice at week 6 PI were used as reference FC maps. A pixel's value in a similarity map was the resulting similarity metric when that pixel's location was used as the seed to construct the subject specific and reference FC maps. The Pearson R-values of the similarity maps were converted to Fisher z-measures.

The homotopic connectivity (HC) metric was obtained by calculating the Pearson's correlation coefficient between a seed's time trace and the time trace of the seed's homolog in the contralateral hemisphere. Pearson R-values were then converted to Fisher z-measures. HC maps can be obtained by plotting HC for every pixel in the FOV. HC maps are necessarily symmetric, so HC maps were visualized in the right (injured) hemisphere.

FC contours were calculated by placing seeds in contralesional (left) hemisphere to generate FC maps. The ipsilesional (right) hemisphere of the FC maps was then thresholded at 50% of a relative or constant maximum. For relative FC contours, thresholds were set at 50% of the maximum value of the group-average map for each week for each network. For constant FC contours, the thresholds were set at 50% of the constant maximum value at week 4 PI for each network. Displaced functional connectivity (dFC) was calculated by using the relative contours as regions of interest in individual mice and averaging the Fisher z-transformed correlation values of all the pixels within the contour. The group-average dFC was calculated.

Group-average zero-lag correlation maps were generated for the sagittal sinus (SS), motor right, and barrel right seeds. This analysis was performed on oxygenated hemoglobin data that had been filtered to the FC band but only had the average signal from each brain hemisphere regressed from it and not the SS seed. The average correlation between the SS and both the motor right and barrel right seeds was calculated.

Calculations of average power. The average oxygenated hemoglobin signal power in the frequency range corresponding to three frequency bands (0.01 Hz–0.04 Hz, 0.04 Hz–0.08 Hz, and 0.08 Hz–0.12 Hz) was computed for every pixel within our field of view (FOV) as described.[21] This analysis was performed on oxygenated hemoglobin data that was collected at ~30 Hz, unfiltered, and did not have the average signal from each brain hemisphere regressed from it. Comparisons of power maps at week 4 and week 6 PI were performed with and without regressing the SS seed.

Mouse lag analysis. Regional-lagged correlation was performed by cross-correlating every pixel's time trace with the time trace of that pixel's contralateral homologue and measuring the time shift associated with peak correlation using MATLAB's *xcorr* function. This analysis was performed on oxygenated hemoglobin data that had been filtered over 0.009 Hz to 0.08 Hz without any signal regression. Mean lag maps were created for each mouse by calculating the average lag across each mouse's imaging session in 5-min increments.

Mouse tumor volume quantification. Hyperintensities in T2-weighted MR images were used to manually segment tumor area in each slice using ImageJ software (National Institutes of Health). Slice tumor volumes were calculated by multiplying tumor area by the slice thickness. When tumors were present in multiple slices, total tumor volume was estimated by summing all slice tumor volumes.

Mouse MRI and OIS co-registration and lesion segmentation. The rostrocaudal and mediolateral resolutions were 1 mm and 125 μm, respectively, for MRI, while the resolution in both directions for OISI was approximately 225 μm based on a Gaussian smoothing kernel with a standard deviation of 1.2 pixels and a pixel size of 78 μm. Therefore, cubic interpolation was used on the MRI images to make the resolutions of MRI and OISI equivalent. To transform the 3D MRI images into 2D images in the same plane as the OISI

images, the maximal voxel intensity value in the ventrodorsal direction was projected to the horizontal plane. The maximum intensity projection (MIP) image was then affine-transformed to a common atlas space using lambda and bregma as landmarks. To segment tumor regions, the MIP images were normalized by subtracting the average intensity value in a 30 pixel by 30-pixel square in each contralesional hemisphere and dividing every pixel by the difference between maximum intensity and the value that was subtracted. Next, every pixel with intensity values below 0.35 were set to zero and the rest of the pixel were set to one. The largest contiguous region of non-zero pixels is designated as tumor (Figure 4(a)).

Human patient methods

Subject enrollment. Inclusion criteria included: newly diagnosed primary brain tumor; age above 18 years; clinically indicated MRI scan as determined by the treating neurosurgeon. Additionally, we required the patient have an R-fMRI scan. Exclusion criteria included: prior brain tumor surgery, or an MRI scan not performed at WU; 30 patients met these criteria.

Human R-fMRI acquisition. All patients were scanned using a Washington University School of Medicine Siemens (Erlangen, Germany) 3T Tim-Trio scanner with a 12-channel head coil. Structural scans included: (1) a sagittal T1-weighted MP-RAGE (TR = 1950 ms, TE = 2.26 ms, flip angle = 90 °, voxel size = 1.0 × 1.0 × 1.0 mm); (2) a transverse T2-weighted turbo spin-echo (TR = 2500 ms, TE = 435 ms, voxel-size = 1.0 × 1.0 × 1.0 mm); and (3) 2D FLAIR (fluid-attenuated inversion recovery) (TR = 7500 ms, TE = 326 ms, 3 mm slices and1.5 × 1.5 mm in-plane resolution). Resting state functional scans were acquired with a gradient echo EPI sequence (TR = 2200 ms, TE = 27 ms, 32 contiguous 4 mm slices, 4 × 4 mm in-plane resolution, total time of 12 min) during which participants were instructed to fixate on a small cross in a low luminance environment.

Human tumor segmentation and region of interest definition. Tumors were manually segmented using Analyze (www.mayo.edu) by inspection of the structural images (T1-weighted post enhancement, T2- weighted, FLAIR), simultaneously displayed in atlas space. All segmentations were reviewed by an experienced neuroradiologist (J.S. Shimony) with special attention to distinguishing glioma from surrounding vasogenic edema.

Two additional related regions of interest were generated. A 'peri-tumoral' region was identified by dilating the tumor by 10 mm and then excluding any voxels within the tumor or outside of the brain. A 'non-tumor' region included all voxels in the ipsilateral hemisphere to the tumor, but not including the tumor or peri-tumoral region.

Human R-fMRI data preprocessing. R-fMRI data underwent preprocessing as described[22] and detailed in the supplementary materials section.

Data underwent additional preprocessing steps: (6) temporal bandpass filtering, retaining frequencies between 0.01–0.1 Hz, (7) removal of spurious variance through regression of 12 parameters of head motion (six parameters obtained by rigid body motion correction, as well as their derivatives), 2 ventricle regions of interest, and 2 white matter regions of interest, and (8) flagging of frames with a framewise displacement > 0.5 mm to be excluded from the R-fMRI computations.[23] A shift mask was then generated by removing frames proceeding or after excluded frames. A minimum of 120 usable frames was required for subject inclusion. Thus, 3 out of 30 patients were excluded. In the retained data, on average, 402 out of 439 frames remained in the included patients.

Human R-fMRI lag processing and analysis. For every brain voxel, lag was calculated relative to the 'homotopic' reference voxel in the opposite hemisphere. The homotopic reference voxel was determined by flipping about the X-axis in atlas space. Lagged cross-correlation analysis was performed for each voxel over the range ±5 TRs (±2.2 seconds) as previously described[22] and detailed in the supplementary materials section.

Statistical analysis

All statistical comparisons were performed using MATLAB (Mathworks). Statistical tests were performed to determine if there was a significant linear relationship between the logarithm of BLI signal and the mean similarity across individual mouse brains or the logarithm of BLI signal and HC for all seeds. Multiple comparisons were corrected using the false discovery rate method ($P < 0.05$, corrected) for pixel by pixel HC map analysis and the Bonferroni method ($P < 0.05$, corrected) for all other instances. Statistical significance was determined by two-tailed unpaired or paired Student's t tests. One sample t-test analysis was used to test whether lags in human data were significantly different from a zero-mean distribution.

Results

Glioma growth disrupts FC

We stereotactically implanted a human GBM cell line (U87-GL) into the right forepaw somatosensory cortex of nude mice ($n = 13$, Figure S1(a)). We chose this cell

line because it grows in a circumscribed manner without infiltration or dissemination throughout the brain. We injected into the right forelimb somatosensory cortex because it borders motor and hindlimb regions. This approach enabled us to identify effects of tumor growth on connectivity both proximal and distal to the injection site without the complication of secondary, infiltrative, or metastatic tumor.

We utilized multiple imaging modalities to assess tumor growth and changes in FC (Figure S1(b)). Placement of the cranial window and OISI was delayed until one week PI to allow the burr hole to heal. FC network structure was monitored using fcOIS. Anatomical tumor volume was quantified longitudinally using magnetic resonance imaging (MRI). Potential CBF alterations due to tumor growth were monitored using LSCI in the third and sixth week PI. We sacrificed the mice in the eight week via transcardial perfusion and performed histology.

BLI provided a non-invasive, validated measure of tumor burden[12] (Figure S2(a)). BLI signal grew exponentially from week to week (Figure S2(b)), confirming the expected cell proliferation trajectory. Complementary to the BLI results, MRI (Figure S2(c)) quantification of tumor volume in a subset of mice ($n = 6$) shows a trend that tumor volume increases with the passage of time (Figure S2(d)).

Group-average FC maps ($n = 13$) constructed with oxygenated hemoglobin traces provided a robust representation of the effect of glioma growth on FC (Figure 1). Since the gliomas could displace functional regions on the ipsilateral brain hemisphere, only FC maps for seeds in the brain hemisphere contralateral to the injection site are displayed. FC maps for seeds in the brain hemisphere ipsilateral to the injection site are provided in Figure S3. Additionally, group-average FC maps ($n = 20$) from sham-injected mice showed reduced FC near the injection. FC recovered with time and normalized by week 4 PI (Figures S4 and S5). Since we were interested only in the effects of tumor growth on FC, we analyzed FC maps starting in week 4 PI. Thus, only group-average FC maps from week 4 PI onward are displayed in Figure 1. In general, functional connections between the two hemispheres declined as time progressed after week 4 PI. Of the networks assessed, only the retrosplenial network maintained symmetry throughout the duration of the experiment. Group-average FC maps constructed with deoxygenated hemoglobin (Figure S6) or total hemoglobin (Figure S7) traces showed similar results.

Changes in FC metrics correlate with tumor burden

A challenge of working with FC data is the multitude of brain maps generated by different seed locations. To reduce this complexity, we calculated a single FC similarity metric for each pixel. The FC similarity metric was generated by correlating the topology of experimental FC maps with a reference FC map.[20] Group-average FC similarity maps exhibited global disruptions in FC (Figure 2(a)). There was an inverse relationship between global FC similarity and the logarithm of the BLI signal (Figure 2(b)).

We also assessed connections between a seed location and its homotopic counterpart (Figure 3(a)). Homotopic connectivity (HC) maps rely on the fact healthy FC maps exhibit a high degree of symmetry. HC has been shown in other applications to be strongly correlated with behavioral deficits and recovery.[24–26] In glioma-injected mice, two large regions showed significant reduction in HC between weeks 4 and 6 (t-test, $p < 0.05$, FDR corrected) – one near the injection site and one remote. Focusing only on HC between seeds provided a localized assessment of connectivity structure (Figure 3(b)). The motor, barrel, parietal and visual networks exhibited a significant ($p < 0.05$, Bonferonni corrected) loss of HC at week 6 PI compared to week 4 PI. Conversely, in sham-injected mice, HC in regions near the injection site significantly increased during the early time points after the injection then remained stable during the later time points (Figure S8). To establish a relationship between FC disruption and tumor burden further, we correlated HC measures for each seed at all time points with the corresponding BLI measure (Figure 3(c)). There was a significant anti-correlation ($p < 0.05$, Bonferonni corrected) between log BLI signal and HC for the motor, forelimb, hindlimb, barrel, and visual seeds. These findings indicate FC in some parts of the brain is more susceptible to the effect of glioma growth than others and both local and remote regions are affected. The residuals for the linear regressions for both similarity and HC appear randomly distributed about zero, suggesting the linear regression model is valid (Figure S9).

Glioma growth causes local and remote FC disruptions

Since the HC maps suggest glioma growth has region-specific effects on FC, we examined the spatial relationship between tumor location and topology of FC disruption. To accomplish this, we developed methods to co-register MRI and OIS data (Figure 4(a)). We then generated tumor frequency maps for the subset of mice with MRIs ($n = 6$) to show the spatial distribution relative to a reference OIS image (Figure 4(b)). Since there is a region in the center of tumor frequency map where all six tumors are present, the stereotaxic injection was likely in a consistent location. The pixel by pixel t-test (Figure 4(c)) map between group-average HC maps

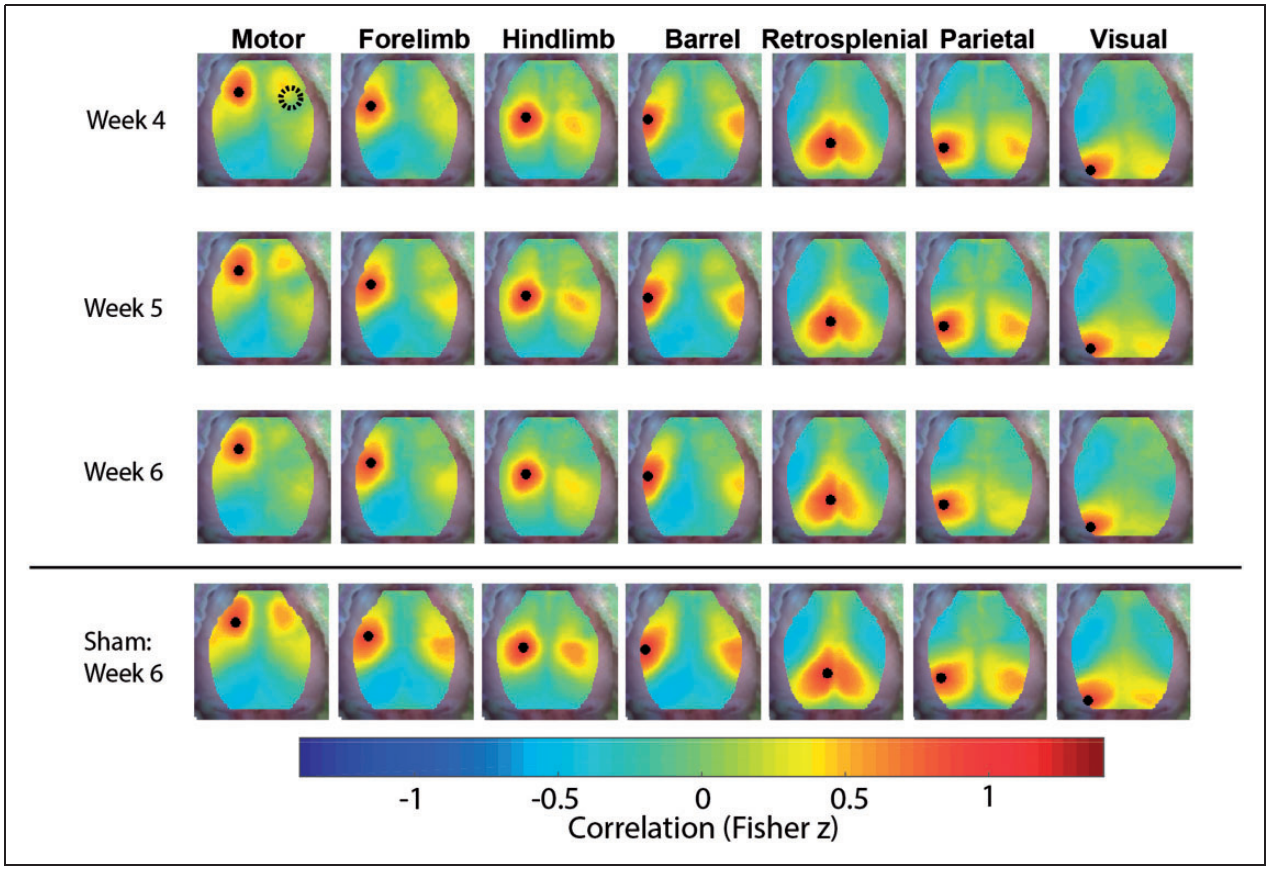

Figure 1. FC maps. Group-average functional connectivity maps constructed with oxygenated hemoglobin traces of mice injected with glioma cells ($n = 13$) for the fourth, fifth and sixth weeks post-injection. Maps demonstrate a loss of symmetry over time. Group-average functional connectivity maps of mice with sham injections ($n = 20$) for the sixth week post-injection are included for reference. Only functional connectivity maps for seeds in the left hemisphere contralateral to the injection site are displayed (the black dots indicate the location of the seed used to construct the functional connectivity map).

($n = 13$) at week 4 and week 6 PI was used to indicate regions of the brain with disrupted FC. An overlay of the map of disrupted FC and non-zero tumor frequency pixels masked by the FOV of OISI showed there were both local and remote regions of disrupted FC (Figure 4(d)). Interestingly, there was an absence of tumor cells in the remote region of disrupted connectivity, as indicated by H&E staining (Figure 4(e)).

Displacement does not account for remote FC disruptions

Gliomas can affect FC maps by either reducing the magnitude of FC between nodes or displacing the location of nodes in space.[4,27] However, the HC and similarity metrics cannot differentiate between these two effects. To distinguish displacement from reductions in the magnitude of FC, we analyzed FC contours (Figure 5(a)). Relative FC contours showed functional regions moved as time progressed. Constant FC contours captured the diminished magnitude of FC as time progressed. Both FC contour analyses revealed some functional areas were split into non-contiguous regions as the tumors grew. Because the locations of the functional areas moved as time progressed, we used the relative FC contours as regions of interests to calculate average dFC values in individual mice (Figure 5(b)). When using dFC, which is less sensitive to displacement than HC, only the motor, parietal, and visual networks had significantly ($p < 0.05$) reduced connectivity in glioma-injected mice.

The lack of significant change in dFC for the barrel network suggests FC changes local to tumor injection site may be caused by displacement. Conversely, the displacement analysis indicates the remote disruption of FC in Glioma mice is not due to displacement of brain tissue. When accounting for displacement in sham-injected mice, FC did not decrease in any networks. FC in hindlimb network actually significantly increased (Figure S10).

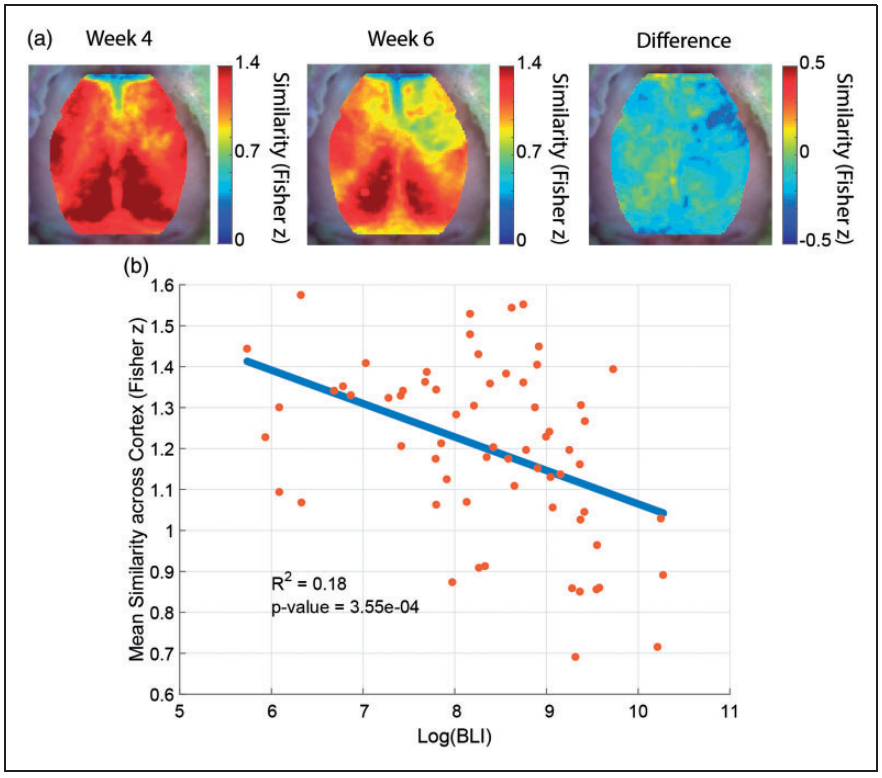

Figure 2. FC similarity metric. (a) Group-average similarity maps of mice injected with glioma cells ($n = 13$). The fourth week post-injection map, the sixth week post-injection map, and the difference map between the fourth and sixth weeks post-injection are displayed. The maps show a global decrease in similarity over time. (b) Scatter plot of the mean similarity across the cortex of individual gliomas at all time point versus the logarithm of bioluminescence signal. Each mouse is represented by more than one point. There is a significant anti-correlation between mean similarity and tumor burden.

Hemodynamic changes contribute to local FC disruptions only

Since measurement of FC with fcOIS is dependent on normal coupling between neural activity and local blood flow, and gliomas are known to have neo-vasculature with abnormal properties,[28] we investigated hemodynamics in the tumor region to determine whether vascular dysregulation influenced our FC results. We compared motor right and barrel right FC maps to the correlation maps for an SS seed (Figure 6(a) and (b)). The SS seed provides a map of the pixels correlated to vascular dynamics. At week 4 PI, neither the motor right seed nor the barrel right seed were correlated with the SS seed. By week 6 PI, the motor right seed had a significantly ($p < 0.05$) increased correlation with the SS seed, while the barrel right seed remained uncorrelated. The increase in correlation between the tumor region and the vasculature (Figure S11) is higher for anterior than posterior portions of the SS. There is also lack of correlation between the anterior SS seed and central and posterior portions of the SS. Since our correlation analysis is all at zero-lag, it is possible both features are due to time lags as blood flows from the anterior to posterior along the SS. Regardless, there is clear synchrony between the tumor region and portions of the vasculature at later time points that is not seen at earlier time points.

To evaluate potential increases in CBF over the tumor, we used LCSI in a subset of glioma-injected mice (Figure 6(c) and (d)) and a subset of sham-injected mice (Figure S12(a) and 12(b)). In the subset of glioma-injected mice ($n = 3$), the LCSI data suggest CBF is increased in the center of the tumor region. However, the LCSI data and MRI data ($n = 6$) are from mutually exclusive subsets of all of the glioma-injected mice ($n = 13$). Therefore, the size and location of the CBF increase maybe biased by the small number of mice imaged. When we quantify CBF in the somatosensory hindlimb region in the right hemisphere, there is a significant ($p < 0.05$) increase from week 3 to week 6 PI. CBF measurements in the somatosensory hindlimb region in the left hemisphere and the visual regions in both hemispheres were unchanged as time progressed. Furthermore, in the subset of sham-injected mice ($n = 3$), neither the left and right somatosensory regions nor the left and right visual regions were significantly changed from week 3 to week 6 PI.

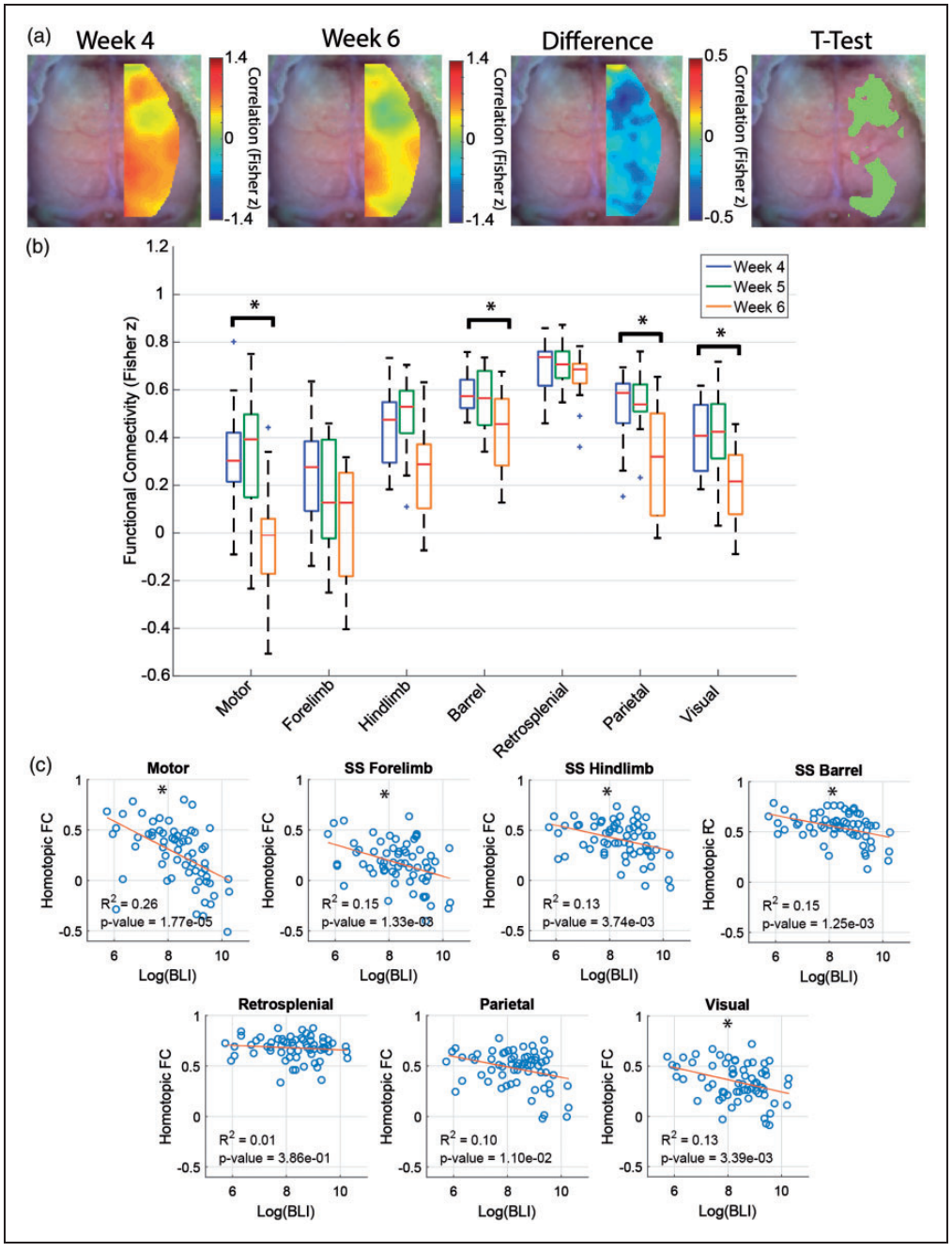

Figure 3. Homotopic connectivity metrics. (a) Group-average homotopic connectivity maps of mice injected with glioma cells ($n = 13$) for different weeks. The fourth week post-injection map, the sixth week post-injection map, and the difference and *t*-test (paired, $p < 0.05$, FDR corrected) maps between the fourth and sixth weeks post-injection are displayed. The maps show that functional connectivity in some regions of the brain is more disrupted than others. (b) Quantification of group-average homotopic connectivity of glioma-injected mice ($n = 13$) for seven homotopic seed pairs within our field of view (paired, *indicates $p < 0.05$, Bonferroni corrected). (c) Scatter plot of homotopic connectivity of glioma mice at all time points versus the logarithm of bioluminescence signal. Each mouse is represented by more than one point. Homotopic connectivity pairs in specific brain regions show significant anti-correlations with tumor burden (*indicates $p < 0.05$, Bonferroni corrected).

To evaluate spectral content of spontaneous hemodynamics, we constructed maps of average power over three frequency bands. The first two bands are over the canonical FC band (0.009 Hz–0.08 Hz), which has been shown to reflect underlying neural activity.[6,9,29] The third band is slightly higher (0.08 Hz–0.12 Hz), which has been attributed to fluctuations of vascular origin[21] and has been shown to have increased power in a case

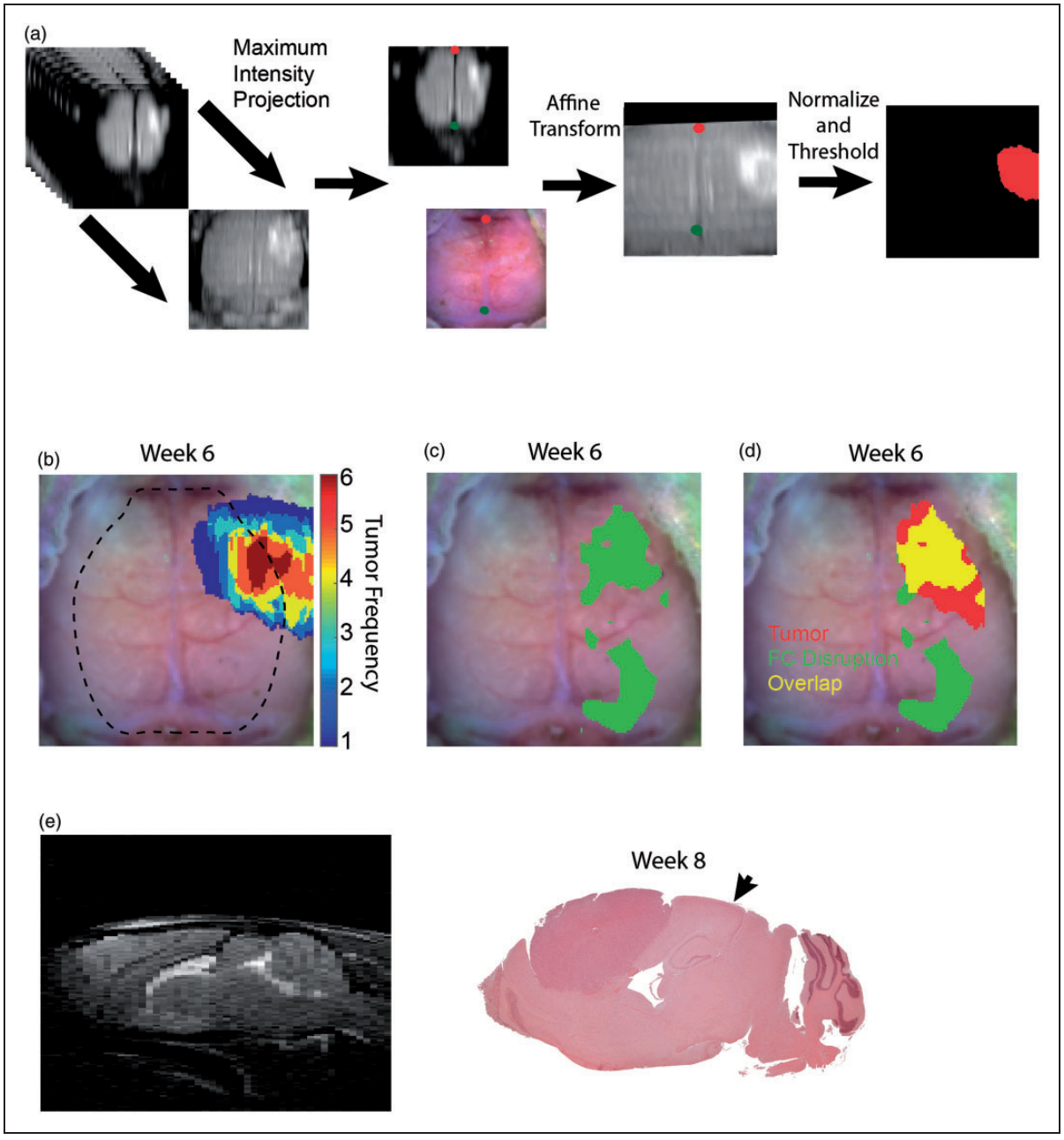

Figure 4. MRI and OIS co-registration, tumor and disrupted functional connectivity overlay, and histology. (a) A maximum intensity projection of T2-weighted MRIs along the ventrodorsal direction was used to project MRIs onto the same plane as OIS, and affine transform was used to co-register the maximum intensity projection image and OIS using fiducial landmarks (the green and red dots indicate lambda and the intersection of the coronal and sagittal sutures, respectively). Images were then normalized and thresholded at 0.35. (b) Frequency map of brain tumors ($n = 6$) that were segmented from co-registered MRIs in sixth week post injection (dotted line indicates field of view of OIS). (c) Map of disrupted functional connectivity constructed by performing a pixel-wise *t*-test between fourth and sixth week post-injection group-average homotopic connectivity maps ($n = 13$, paired, $p < 0.05$, FDR corrected). (d) Overlay of the non-zero tumor frequency pixels masked by the FOV of OIS and map of disrupted functional connectivity. Overlay image demonstrates local and remote regions of functional connectivity disruption. (e) Hematoxylin and eosin stain of representative mouse injected with glioma cells in the eigth week post-injection (MRI provides orientation). Histology indicates that the tumors are well-circumscribed, localized to the injection site, and absent from the region of remote functional connectivity disruption (arrow indicates the remote region of functional connectivity disruption corresponding to the visual cortex).

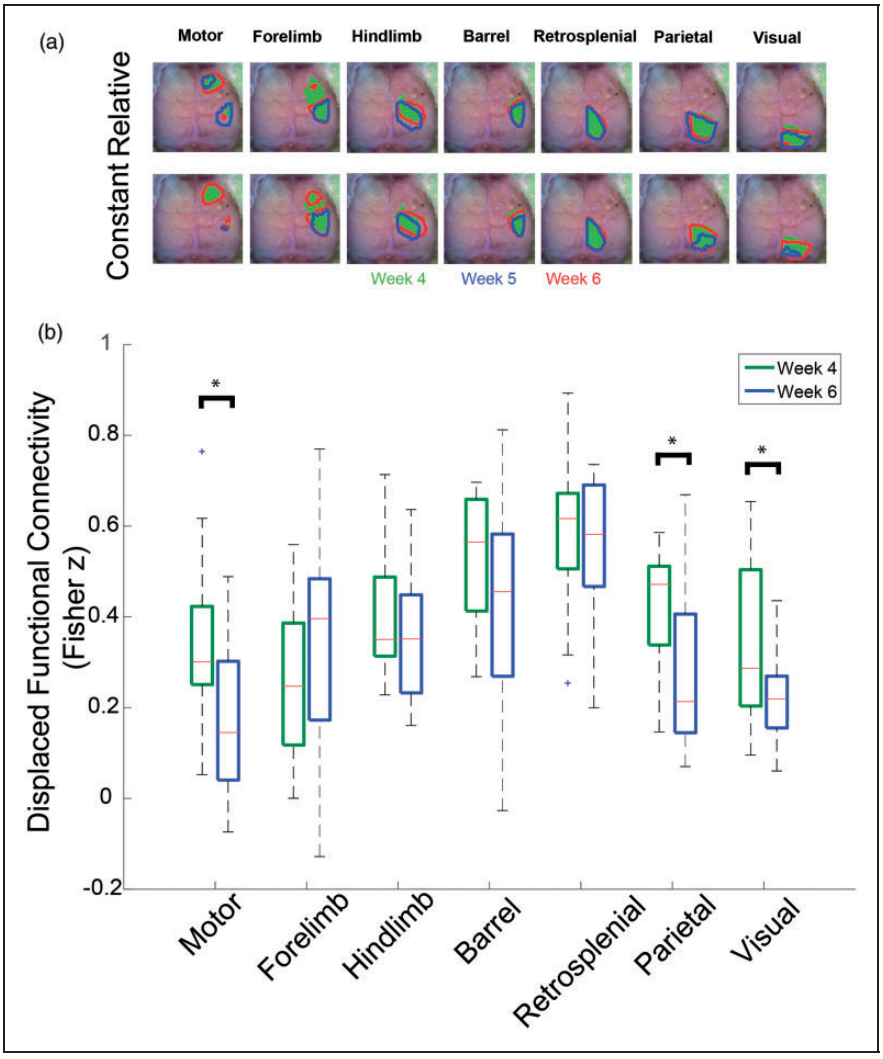

Figure 5. Functional connectivity contours and displaced functional connectivity. (a) Group-average functional connectivity contours of 50% of relative and constant maximums ($n = 13$) for different weeks. Relative functional connectivity contours use a threshold based on 50% of the maximum of each week. Constant functional connectivity contours use a threshold based on 50% of the maximum at week 4 post-injection (Green = Week 4, Red = Week 5, and Blue = Week 6). The contours indicate that some functional regions are displaced, and even split, by the tumor. Constant maximum contours show that functional regions decrease in area over time. (b) Quantification of the group-average displaced functional connectivity ($n = 13$) for week 4 and week 6 post injection (*indicates $p < 0.05$). Displaced functional connectivity is calculated by using the relative functional connectivity contours as regions of interest and averaging all the Fisher z correlation values within each contour. Only the motor and visual functional regions have decreased magnitude when accounting for displacement.

study of a human undergoing glioma resection[30] (Figure 6(e)). Average power maps for glioma-injected mice revealed the average power in all frequency bands declined globally across the cortex between week 4 and week 6 PI. However, in the 0.01 Hz–0.04 Hz frequency band, average power relative to the whole brain increased in a focal region near the injection site. After the SS seed was regressed out, the average power in all frequency bands decreased globally over the cortex. In the 0.01 Hz–0.04 Hz frequency band, this affected the peri-injection site region most strongly. This suggests this focal power increase was being driven by a signal of vascular origin. These findings indicate gliomas cause local vascular dysregulation that confounds proximal FC measurements. Conversely, vascular dysregulation was absent from regions remote from the glioma. Therefore, FC disruptions in remote regions are likely due to changes in neural activity.

To further investigate the cause of observed changes in connectivity, we measured hemodynamic delays relative to the contralateral hemisphere. We performed a

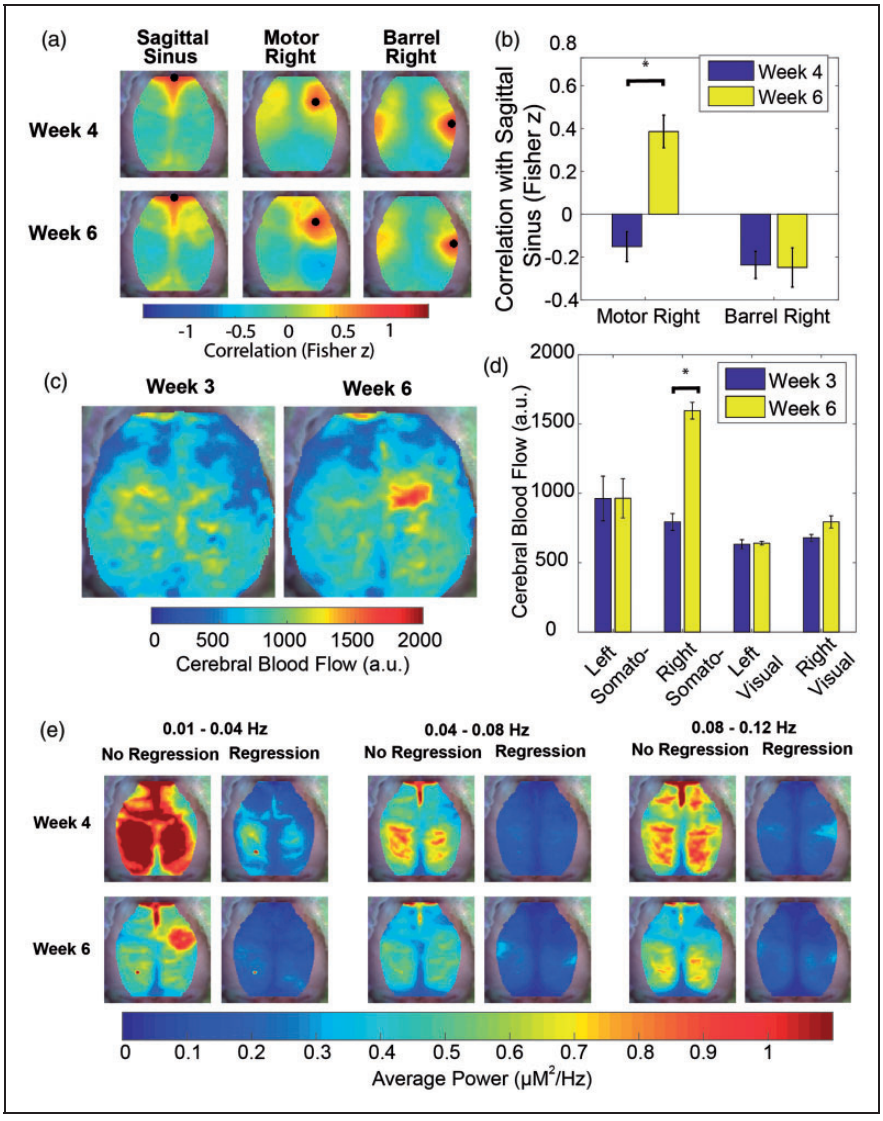

Figure 6. Vascular dysregulation within the tumor region. (a) Group-average correlation maps ($n = 13$) of sagittal sinus, motor right and barrel right seeds at week 4 and week 6 post-injection. (b) Quantification of the group-average correlation ($n = 13$) between the sagittal sinus seed and both the motor right and barrel right seeds (*indicates $p < 0.05$). This graph indicates that regions near the injection site become correlated with systemic vascular fluctuations over time. (c) Group-average cerebral blood flow maps for a subset of mice ($n = 3$) at week 3 and week 6 post injection. (d) Quantification of the group-average cerebral blood flow value ($n = 3$) for the left and right somatosensory hindlimb and left and right visual seeds at week 3 and week 6 post-injection indicates that tumor blood flow increases over time. (e) Group-average power maps ($n = 13$) for three frequency bands with and without regression of the signal from a vascular feature (sagittal sinus seed) at week 4 and week 6 post-injection demonstrate that average power maps decrease in magnitude with time and with regression of the sagittal sinus. However, average power in the tumor region increases in the 0.01 Hz–0.04 Hz frequency band when there is no regression of the sagittal sinus. The power in the tumor region is affected more profoundly by sagittal sinus regression than other regions indicating that the hemodynamic in this region is likely being driven by vascular fluctuations of systemic origin.

lag analysis by cross-correlating the time trace of every pixel with the time trace of its contralateral homolog and mapping the time shift that maximized the cross-correlation value (Figure7(a) and (b)). Lags between tumor tissue in the somatosensory region and its homotopic region were significantly increased at week 6 compared to week 4 PI. Homotopic lags between visual seeds were not significantly different between week 4 and week 6 PI. Again, changes in cerebral hemodynamics were observed only in areas directly proximal to the tumor and not in the distant visual cortex in which FC was substantially altered.

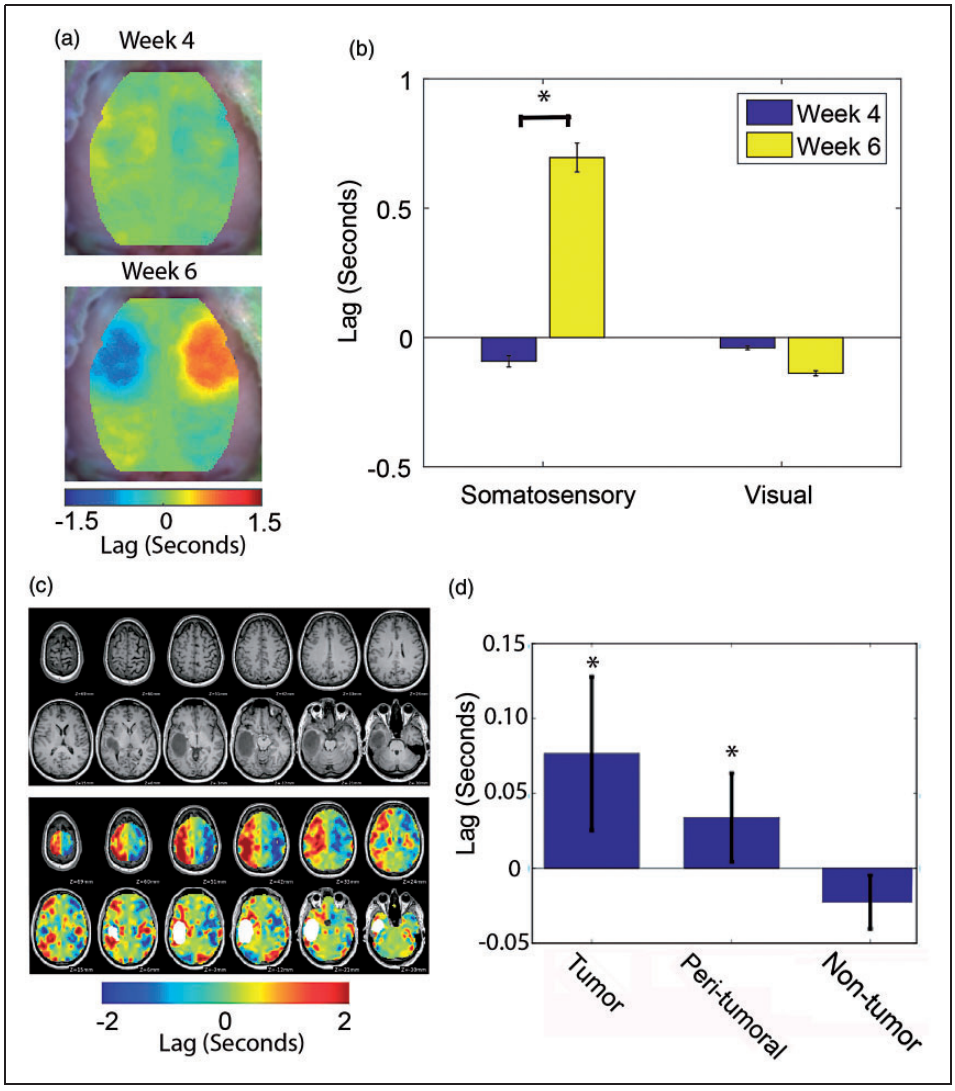

Figure 7. Homotopic lags in mice and in humans. (a) Group-average homotopic lag maps for mice injected with glioma cells ($n = 13$) at week 4 and week 6 post injection. (b) Quantification of the group-average homotopic lag ($n = 13$) for the somatosensory forelimb and visual seeds (*indicates $p < 0.05$). These data indicate that murine tumor hemodynamics lag behind the homotopic brain region. (c) Structural MRIs and homotopic lags for a representative human case. (d) Quantification of the group-average homotopic lag ($n = 27$) for the tumor, peri-tumoral, and non-tumor brain regions (*indicates $p < 0.05$). Tumor and peri-tumoral regions, but not the non-tumor region, exhibit significant lags compared to their homotopic regions.

Human hemodynamic findings are recapitulated in the mouse model

To confirm that the findings from our mouse model apply across species (mouse to human) and across imaging modalities (fcOIS to fcMRI), we analyzed R-fMRI data in a cohort of 27 patients diagnosed with brain gliomas (WHO grades II, III, and IV). We measured hemodynamic lags in all voxels based on a homotopic reference seed. We found the area proximal to the tumors frequently showed substantial homotopic lags (Figure 7(c)). To quantify this observation, we generated three regions: tumor, peri-tumoral, and non-tumor. Across patients, lags for the tumor and peri-tumoral regions were significantly different from a distribution with a zero mean, while lags for the non-tumor region were not (Figure 7(d)). These results show alterations to perilesional vasculature observed in our mouse model are an accurate representation of changes occurring in human gliomas.

Discussion

In this study, functional disruption was examined in a mouse model of GBM through longitudinal measurements of FC, tumor growth, bioluminescence, and

CBF. Gliomas were found to disrupt FC in a manner that correlated with the degree of tumor burden as measured by both cell count (BLI) and macroscopic structural measures of volume (MRI). Although the R^2 values that we obtained are low, they are similar to R^2 values (0.16 to 0.389) in previously published studies in which FC was correlated with measures of pathology,[11,24,31] suggesting there is some relationship (whether it be linear or non-linear) where FC decreases as tumor burden increases. Additionally, gliomas cause local hemodynamic changes (i.e. increased CBF, increased low frequency power, and increased temporal lag relative to the unaffected hemisphere) that could contribute to measures of FC disruption.

There are many similarities between our mouse data and reported studies on human subjects. First, in humans, gliomas disrupt interhemispheric FC, especially between homotopic regions.[2] In healthy mammals, homotopic brain regions exhibit a high degree of FC.[5,9,32,33] Human ischemic stroke studies have shown connectivity between homotopic regions is most vulnerable to brain injury and HC correlates best with both the degree of deficit and the degree of recovery.[24–26] In the setting of human gliomas, interhemispheric connections are most consistently weakened.[2] In our mouse study, we found tumor growth significantly affects HC (Figure 3(a) and (b)). Second, in humans, gliomas can displace functional regions while maintaining FC strength.[4,27] The phenomenon of displacement has also been observed in functional region mapping done for neurosurgical planning.[4,34] Gliomas in our mouse model were also found to displace functional regions, as indicated by the barrel network having significantly reduced HC with the passage of time, but not significantly different dFC. Third, in humans, gliomas can have remote effects on FC.[35,36] In the present study, gliomas in the forelimb somatosensory cortex disrupted FC in the parietal and visual cortices. Disruption of the FC of the parietal and visual regions persisted even when displacement was taken into consideration (Figure 5(b)). Additionally, the gliomas in this study exhibited a well-circumscribed pattern of growth and tumor cells were absent from the parietal and visual cortices (Figure 4(e)). Furthermore, hemodynamic alterations were confined to the region near the injection site. These findings suggest the disturbances in local neural activity of somatosensory regions underlie remote functional disruptions in the parietal and visual regions. Related findings of FC connections between the somatosensory cortex and visual system have been reported in hierarchical organization studies of human FC.[37] Fourth, in humans, high-grade gliomas have altered hemodynamics as a consequence of their abnormal neo-vascularity.[28] This results in increased cerebral blood volume and CBF in the region of neoplastic tissue.[38] Additionally, neurovascular uncoupling can result from the abnormal blood vessels.[39,40] Our results indicate murine and human tumors can exhibit significant hemodynamic lags likely due to abnormal neo-vascularity (Figure 7). Our mouse model recapitulates the hemodynamic dysregulation seen in human tumors. The mouse model has increased CBF in the region of neoplastic tissue (Figure 6(c) and (d)). Furthermore, there was neurovascular uncoupling such that the tumor region acquired hemodynamics similar to known vascular regions (Figure 6(a) and (b)). Thus, we conclude that our mouse model is a valid paradigm for studying glioma-associated FC change.

This mouse model has the potential to illuminate mechanisms of glioma-associated FC change and development of functional deficits. Studies have shown FC correlates with cognitive performance in the setting of normal aging[41] and stroke.[24] Furthermore, there have been several studies using magnetoencephalography showing FC correlates with performance on cognitive tests in glioma patients.[42,43] A recent study using fcMRI showed FC in different networks correlated with performance on multiple cognitive tests in glioma patients.[3] Moreover, FC could inform treatment options. There is a growing research effort to use FC in pre-surgical mapping of eloquent cortex.[4,44] Additionally, FC may determine who would be good candidates for cognitive therapy.[45]

Gliomas cause local hemodynamics changes that may confound interpretation of FC analysis. FC is measured by correlating fluctuations in hemoglobin-based signals. For these hemoglobin-based signals to reflect underlying neural activity accurately, neurovascular coupling (NVC) must be intact. Gliomas can affect local NVC in multiple ways. Glioma cells can displace astrocyte end-feet from blood vessels.[46] Glioma cells release growth factors that stimulate blood vessels to grow in an abnormal, tortuous manner.[28] For FC to be established in the setting of glioma growth, robust methods for the detection of neurovascular uncoupling must be applied. To date, cerebrovascular reactivity mapping and measurements of perfusion and blood volume have been used for this purpose in glioma patients.[39,47] In stroke patients, hemodynamic lags have been used to detect neurovascular uncoupling.[22] Our mouse model will be useful for validating methods of neurovascular uncoupling detection because it recapitulates the hemodynamic changes seen in human glioma patients.

One of the limitations of this study is that assessments of FC with fcOIS are restricted to superficial structures of the cortex due to light scattering. Therefore, viable brain tissue that has been displaced ventrally by growing gliomas may have artificially lower FC because the tissue has moved out of the FOV of the OISI system. Additionally, fcOIS cannot

map FC of subcortical structures, such as the thalamus, which could provide clues about the origin of the remote FC disruption. Optically based whole-brain assessments of FC are still possible using diffuse optical tomography methods. Our lab has recently shown the feasibility of such methods in vivo.[48] A second limitation of this study is that the injection injury causes measurable disruptions to FC on its own. Therefore, subtle changes in FC near the injection site during the early stages of glioma growth may be difficult to detect. However, the magnitude of the effect of late stage glioma growth on local FC was far greater than the injury effect and easily measured. A third limitation of this study is that we did not collect data from awake mice. Ketamine/xylazine cocktails can cause changes in a number of physiologic parameters, including reducing CBF[49,50] and heart rate.[51] Consequently, the magnitude of the increase in CBF in the tumor could be blunted. Additionally, the ketamine/xylazine cocktail could have differential effects on tumor and normal vasculature; thus, either increasing or decreasing the contrast between the tissues. We plan to study the effects of anesthesia on our mice in the future.

This model will enable a wide range of future studies to address how tumor characteristics, such as circumscribed versus infiltrative patterns of growth, growth in different brain regions, or growth at different stages of brain development, differentially affect FC changes. Given that FC can reflect polysynaptic network communication,[33] it will be important to implement the above manipulations with methods capable of measuring more direct, monosynaptic connections between regions using optogenetics.[15] This pairing would inform how focal lesions differentially affect network communication as has been performed following stroke.[52] Lastly, we could perform studies in mice expressing genetically encoded calcium indicators, such as GCaMP[14] to assess and validate the effects of gliomas on neural activity and NVC.

Funding

The author(s) disclosed receipt of the following financial support for the research, authorship, and/or publication of this article: This work was supported in part by National Institutes of Health Grants T32GM007200 (to IEO and JSS), R01NS078223 (to J.P.C), R01NS084028 (to JPC), R01NS099429 (to JPC), K25NS083754 (to AQB), P50CA094056 (Molecular Imaging Center, Mallinckrodt Institute of Radiology, Washington University School of Medicine), Eunice Kennedy Shriver National Institute of Child Health & Human Development of the National Institutes of Health under Award U54 HD087011 to the Intellectual and Developmental Disabilities Research Center at Washington University in St. Louis (to JPC and JS Shimony), and the Children's Discovery Institute (to JBR).

Acknowledgments

We thank Sam Achilefu, Bradley Schlaggar, and Abraham Synder for critical discussions of the manuscript and the data. Lynne Marsala and Julie Prior and the Molecular Imaging Center and Oncologic Imaging Program of the Siteman Cancer Center assisted with bioluminescence imaging (BLI). Scott Beeman assisted with magnetic resonance imaging, and Ron Perez and the Hope Center Animal Surgery Core assisted with cell injections.

Declaration of conflicting interests

The author(s) declared no potential conflicts of interest with respect to the research, authorship, and/or publication of this article.

Authors' contributions

IEO, JSS, AQB, JSS, JBR, and JPC designed the study. IEO, JSS, NMW, GAB performed experiments. IEO and JSS analyzed data. IEO, JSS, AQB, JSS, JBR, and JPC wrote the manuscript.

Supplementary material

Supplementary material for this paper can be found at the journal website: http://journals.sagepub.com/home/jcb

References

1. Ghinda DC, Wu J-S, Duncan NW, et al. How much is enough – Can resting state fMRI provide a demarcation for neurosurgical resection in glioma? *Neurosci Biobehav Rev* 2018; 84: 245–261.
2. Otten ML, Mikell CB, Youngerman BE, et al. Motor deficits correlate with resting state motor network connectivity in patients with brain tumours. *Brain* 2012; 135: 1017–1026.
3. Maesawa S, Bagarinao E, Fujii M, et al. Evaluation of resting state networks in patients with gliomas: connectivity changes in the unaffected side and its relation to cognitive function. *PLoS ONE* 2015; 10(2): e0118072. https://doi.org/10.1371/journal.pone.0118072.
4. Zhang D, Johnston JM, Fox MD, et al. Preoperative sensorimotor mapping in brain tumor patients using spontaneous fluctuations in neuronal activity imaged with fMRI: initial experience. *Neurosurgery* 2009; 65: 226–236.
5. Biswal B, Yetkin FZ, Haughton VM, et al. Functional connectivity in the motor cortex of resting human brain using echo-planar MRI. *Magn Reson Med* 1995; 34: 537–541.
6. Fox MD and Raichle ME. Spontaneous fluctuations in brain activity observed with functional magnetic resonance imaging. *Nat Rev Neurosci* 2007; 8: 700–711.
7. Huszthy PC, Daphu I, Niclou SP, et al. In vivo models of primary brain tumors: pitfalls and perspectives. *Neuro Oncol* 2012; 14: 979–993.
8. Zerbi V, Grandjean J, Rudin M, et al. Mapping the mouse brain with rs-fMRI: an optimized pipeline for functional network identification. *Neuroimage* 2015; 123: 11–21.

9. White BR, Bauer AQ, Snyder AZ, et al. Imaging of functional connectivity in the mouse brain. *PLoS One* 2011; 6: e16322.
10. Bero AW, Bauer AQ, Stewart FR, et al. Bidirectional relationship between functional connectivity and amyloid-β deposition in mouse brain. *J Neurosci* 2012; 32: 4334–4340.
11. Bauer AQ, Kraft AW, Wright PW, et al. Optical imaging of disrupted functional connectivity following ischemic stroke in mice. *Neuroimage* 2014; 99: 388–401.
12. Rubin JB, Kung AL, Klein RS, et al. A small-molecule antagonist of CXCR4 inhibits intracranial growth of primary brain tumors. *Proc Natl Acad Sci U S A* 2003; 100: 13513–13518.
13. Brooks MD, Jackson E, Warrington NM, et al. PDE7B is a novel, prognostically significant mediator of glioblastoma growth whose expression is regulated by endothelial cells. *PLoS One* 2014; 9: e107397.
14. Wright PW, Brier LM, Bauer AQ, et al. Functional connectivity structure of cortical calcium dynamics in anesthetized and awake mice. *PLoS One* 2017; 12: e0185759.
15. Bauer AQ, Kraft AW, Baxter GA, et al. Effective connectivity measured using optogenetically evoked hemodynamic signals exhibits topography distinct from resting state functional connectivity in the mouse. *Cereb Cortex* 2018; 28: 370–386.
16. Goldhoff P, Warrington NM, Limbrick DD, et al. Targeted inhibition of cyclic AMP phosphodiesterase-4 promotes brain tumor regression. *Clin Cancer Res* 2008; 14: 7717–7725.
17. Beeman SC, Shui Y-B, Perez-Torres CJ, et al. O2-sensitive MRI distinguishes brain tumor vs. radiation necrosis in murine models. *Magn Reson Med* 2016; 75: 2442–2447.
18. Bergonzi KM, Bauer AQ, Wright PW, et al. Mapping functional connectivity using cerebral blood flow in the mouse brain. *J Cereb Blood Flow Metab* 2015; 35: 367–370.
19. Franklin K and Paxinos G. *The mouse brain in stereotaxic coordinates*, 3rd ed. New York: Academic Press, 2008.
20. Siegel JS, Snyder AZ, Metcalf NV, et al. The circuitry of abulia: insights from functional connectivity MRI. *Neuroimage Clin* 2014; 6: 320–326.
21. Bumstead JR, Bauer AQ, Wright PW, et al. Cerebral functional connectivity and Mayer waves in mice: phenomena and separability. *J Cereb Blood Flow Metab* 2017; 37: 471–484.
22. Siegel JS, Snyder AZ, Ramsey L, et al. The effects of hemodynamic lag on functional connectivity and behavior after stroke. *J Cereb Blood Flow Metab* 2016; 36: 2162–2176.
23. Power JD, Barnes KA, Snyder AZ, et al. Spurious but systematic correlations in functional connectivity MRI networks arise from subject motion. *Neuroimage* 2012; 59: 2142–2154.
24. Carter AR, Astafiev SV, Lang CE, et al. Resting interhemispheric functional magnetic resonance imaging connectivity predicts performance after stroke. *Ann Neurol* 2010; 67: 365–375.
25. Carter AR, Patel KR, Astafiev SV, et al. Upstream dysfunction of somatomotor functional connectivity after corticospinal damage in stroke. *Neurorehabil Neural Repair* 2012; 26: 7–19.
26. van Meer MPA, van der Marel K, Wang K, et al. Recovery of sensorimotor function after experimental stroke correlates with restoration of resting-state interhemispheric functional connectivity. *J Neurosci* 2010; 30: 3964–3972.
27. Ghumman S, Fortin D, Noel-Lamy M, et al. Exploratory study of the effect of brain tumors on the default mode network. *J Neurooncol* 2016; 128: 437–444.
28. Jain RK, di Tomaso E, Duda DG, et al. Angiogenesis in brain tumours. *Nat Rev Neurosci* 2007; 8: 610–622.
29. Cordes D, Haughton VM, Arfanakis K, et al. Frequencies contributing to functional connectivity in the cerebral cortex in "resting-state" data. *Am J Neuroradiol* 2001; 22: 1326–1333.
30. Rayshubskiy A, Wojtasiewicz TJ, Mikell CB, et al. Direct, intraoperative observation of ~0.1 Hz hemodynamic oscillations in awake human cortex: implications for fMRI. *Neuroimage* 2014; 87: 323–331.
31. Hedden T, Dijk KRAV, Becker JA, et al. Disruption of functional connectivity in clinically normal older adults harboring amyloid burden. *J Neurosci* 2009; 29: 12686–12694.
32. Hutchison RM, Mirsattari SM, Jones CK, et al. Functional networks in the anesthetized rat brain revealed by independent component analysis of resting-state FMRI. *J Neurophysiol* 2010; 103: 3398–3406.
33. Vincent JL, Patel GH, Fox MD, et al. Intrinsic functional architecture in the anaesthetized monkey brain. *Nature* 2007; 447: 83–86.
34. Wunderlich G, Knorr U, Herzog H, et al. Precentral glioma location determines the displacement of cortical hand representation. *Neurosurgery* 1998; 42: 18–26; discussion 26–27.
35. Harris RJ, Bookheimer SY, Cloughesy TF, et al. Altered functional connectivity of the default mode network in diffuse gliomas measured with pseudo-resting state fMRI. *J Neurooncol* 2014; 116: 373–379.
36. Zhang H, Shi Y, Yao C, et al. Alteration of the intra- and cross- hemisphere posterior default mode network in frontal lobe glioma patients. *Sci Rep* 2016; 6: 26972.
37. Lee MH, Hacker CD, Snyder AZ, et al. Clustering of resting state networks. *PLoS One* 2012; 7: e40370.
38. Hakyemez B, Erdogan C, Ercan I, et al. High-grade and low-grade gliomas: differentiation by using perfusion MR imaging. *Clin Radiol* 2005; 60: 493–502.
39. Hou BL, Bradbury M, Peck KK, et al. Effect of brain tumor neovasculature defined by rCBV on BOLD fMRI activation volume in the primary motor cortex. *Neuroimage* 2006; 32: 489–497.
40. Agarwal S, Sair HI, Yahyavi-Firouz-Abadi N, et al. Neurovascular uncoupling in resting state fMRI demonstrated in patients with primary brain gliomas. *J Magn Reson Imaging* 2016; 43: 620–626.
41. Damoiseaux JS, Beckmann CF, Arigita EJS, et al. Reduced resting-state brain activity in the "default

network'' in normal aging. *Cereb Cortex* 2008; 18: 1856–1864.
42. Bosma I, Douw L, Bartolomei F, et al. Synchronized brain activity and neurocognitive function in patients with low-grade glioma: a magnetoencephalography study. *Neuro Oncol* 2008; 10: 734–744.
43. van Dellen E, de Witt Hamer PC, Douw L, et al. Connectivity in MEG resting-state networks increases after resective surgery for low-grade glioma and correlates with improved cognitive performance. *Neuroimage Clin* 2012; 2: 1–7.
44. Lee MH, Miller-Thomas MM, Benzinger TL, et al. Clinical resting-state fMRI in the preoperative setting: are we ready for prime time? *Top Magn Reson Imaging* 2016; 25: 11–18.
45. Mason L, Peters E and Kumari V. Functional connectivity predictors and mechanisms of cognitive behavioural therapies: a systematic review with recommendations. *Aust N Z J Psychiatry* 2016; 50: 311–321.
46. Watkins S, Robel S, Kimbrough IF, et al. Disruption of astrocyte-vascular coupling and the blood–brain barrier by invading glioma cells. *Nat Commun* 2014; 5: 4196.
47. Zaca D, Hua J and Pillai JJ. Cerebrovascular reactivity mapping for brain tumor presurgical planning. *World J Clin Oncol* 2011; 2: 289–298.
48. Reisman MD, Markow ZE, Bauer AQ, et al. Structured illumination diffuse optical tomography for noninvasive functional neuroimaging in mice. *Neurophotonics* 2017; 4: 021102.
49. Ku T and Choi C. Noninvasive optical measurement of cerebral blood flow in mice using molecular dynamics analysis of indocyanine green. *PLoS One* 2012; 7: e48383.
50. Lei H, Grinberg O, Nwaigwe CI, et al. The effects of ketamine-xylazine anesthesia on cerebral blood flow and oxygenation observed using nuclear magnetic resonance perfusion imaging and electron paramagnetic resonance oximetry. *Brain Res* 2001; 913: 174–179.
51. Toyama H, Ichise M, Liow J-S, et al. Evaluation of anesthesia effects on [18F]FDG uptake in mouse brain and heart using small animal PET. *Nucl Med Biol* 2004; 31: 251–256.
52. Lim DH, LeDue JM, Mohajerani MH, et al. Optogenetic mapping after stroke reveals network-wide scaling of functional connections and heterogeneous recovery of the peri-infarct. *J Neurosci* 2014; 34: 16455–16466.